EurJIC
European Journal of Inorganic Chemistry

Chemistry Europe
European Chemical Societies Publishing

Accepted Article

Title: Iron(II)–Schiff Base Complexes as Photocatalysts for Controlled Radical Photopolymerization under LED Irradiation

Authors: Sergio M. M. Yamada, Maria L. B. Figueiredo, Naralyne M. Pesqueira, Felipe Fantuzzi, Valdemiro P. Carvalho-Jr, and Beatriz Eleutério Goi

To be cited as: *Eur. J. Inorg. Chem.* **2025**, e202500096

Link to VoR: https://doi.org/10.1002/ejic.202500096

WILEY VCH

10.1002/ejic.202500096

Iron(II)–Schiff Base Complexes as Photocatalysts for Controlled Radical Photopolymerization under LED Irradiation

Sergio M. M. Yamada[a], Maria L. B. Figueiredo[a,b], Naralyne M. Pesqueira[a], Felipe Fantuzzi[b], Valdemiro P. Carvalho-Jr[a], Beatriz E. Goi[a*]

[a] *São Paulo State University (Unesp), School of Technology and Sciences, Presidente Prudente, SP, 19060-900, Brazil*

[b] *Chemistry and Forensic Science, School of Natural Sciences, University of Kent, Park Wood Rd, Canterbury CT2 7NH, UK*

*Correspondence to: B. E. Goi (E-mail: beatriz.goi@unesp.br)

10.1002/ejic.202500096

Abstract

Photocatalysts, particularly metal-based complexes, have gained significant attention in photoredox catalysis, enabling controlled radical photopolymerization (CRP2) under mild irradiation conditions, such as sunlight or LED bulbs. In this study, three Fe(II) complexes−**Fe^{II}Salen**, **Fe^{II}Saloex**, and **Fe^{II}Salophen**−bearing non-symmetrical Schiff base ligands were synthesized and designed for potential application in CRP2. The complexes were characterized using FTIR, UV-Vis, and fluorescence spectroscopy, MALDI-TOF mass spectrometry, and elemental analysis. Additionally, density functional theory (DFT) and time-dependent density functional theory (TD-DFT) calculations were conducted to extract key structural, electronic, and excited-state properties. The catalytic performance of these Fe(II) complexes in the CRP2 of methyl acrylate (MA) was evaluated under different conditions, using ethyl α-bromophenylacetate (EBPA) as the initiator and triethylamine (TEA) as the electron donor. The photopolymerizations proceeded efficiently, yielding polymers with controlled molecular weights and narrow molecular weight distributions (MWD). Among the tested photocatalysts, **Fe^{II}Saloex** exhibited the best performance, achieving high conversion and low polydispersity under LED irradiation. Furthermore, a mechanism was proposed based on spectroscopic analyses and literature data.

Keywords: iron(II), Schiff base, photopolymerization, CRP2, LED irradiation.

1. Introduction

Polymerization reactions find widespread application across diverse industrial sectors, including coatings,[1] 3D printing,[2] adhesives,[3] dentistry,[4] medicine,[5] microelectronics,[6] and nanomaterial design.[7] In recent decades, controlled/living radical polymerization (CRP) has revolutionized polymer synthesis by endowing precise control over polymer architecture, molecular weight, and functionality. However, conventional CRP methods often impose harsh reaction conditions and lack spatial and temporal control, prompting the emergence of controlled radical photopolymerization (CRP2). This innovative technique harnesses light-induced initiation, offering refined control over polymerization reactions while operating at ambient temperatures, thereby minimizing undesired side reactions.[8,9]

The versatility of CRP2 imparts economic and environmental advantages, such as solvent-free processing, low energy consumption, and rapid reaction times, rendering it highly appealing for industrial applications. This advancement represents a significant departure from classical photoinitiators (PIs), where light merely triggers the reaction. In CRP2, photoinitiating systems (PISs) are employed, whereby light-mediated control over dormant species ensures re-initiation exclusively under irradiation, utilizing light emitting diodes (LEDs) or even sunlight. This nuanced control facilitates diverse applications, including copolymer synthesis, on-demand polymerization, and precise surface patterning with spatial precision.[9,10]

The pursuit of environmentally friendly and efficient technologies has driven the development of PISs for polymerization. To be effective in CRP2, both photocatalysts (PCs) and PISs must possess specific characteristics. The PC should exhibit robust light absorption properties within the visible spectrum to efficiently initiate the photoredox catalysis process under mild irradiation conditions.[10] Additionally, the PC should

possess a suitable redox potential to facilitate the generation of radicals or other reactive species crucial for initiating polymerization reactions. Equally important is the stability and compatibility of the PC with the reaction conditions, ensuring sustained activity throughout the polymerization process while ideally aligning with the principles of green chemistry.[10]

Regarding the polymerization initiation system, its components should work together synergistically to achieve efficient polymerization. The PIS typically includes a photoinitiator—either on its own or in combination with co-initiators—that should exhibit high initiating efficiency and compatibility with the PC. Additionally, it should be meticulously designed to promptly generate active species upon light irradiation, thereby enabling precise control over polymerization kinetics and molecular weight distribution. [11]

Notably, CRP2 can follow two main pathways: an oxidative pathway, based on a PC/iodonium salt/silane (or PC/iodonium salt/N-vinyl carbazole) system, and a reductive pathway, based on a PC/amine/alkyl halide system. In the quest for efficient CRP2 systems, the exploration of various PCs has been paramount. While organic molecules have shown promise as efficient PCs, attention has turned towards metal complexes due to their favourable properties, including strong visible light absorption and redox capabilities.[11]

Metal complexes such as iridium,[12] ruthenium,[13] copper,[14] platinum,[15] and iron[16] have been explored. Among these, iron emerges as a particularly promising candidate, boasting suitable visible light absorption properties and environmental friendliness. Despite its potential, the utilization of iron complexes in photopolymerization processes remains relatively limited compared to other metals.

Therefore, the development of novel Fe-based PISs presents an opportunity to expand the repertoire of CRP2 catalysts, offering enhanced performance and sustainability.[17,18]

Previously, our research team explored various reversible deactivation radical polymerization (RDRP) methodologies, including conventional atom transfer radical polymerization (ATRP)[19-25] and organometallic-mediated radical polymerization (OMRP).[26-30] Additionally, we possess expertise in photoinduced RDRP techniques, employing cobalt, nickel and manganese complexes alongside Schiff base ligands to mediate photo-OMRP reactions across diverse monomers.[31-34] In the present study, we introduce Schiff base–iron(II) complexes for photoinduced, iron-catalyzed CRP2 (Figure 1). These catalysts feature non-symmetric Schiff base ligands coordinated by two oxygen and two nitrogen atoms, and are activated under 365 nm LED irradiation. We evaluated their performance using varied proportions of ethyl α-bromophenylacetate (EBPA) as the initiator, triethylamine (TEA) as the electron donor, and methacrylate (MA) as the monomer.

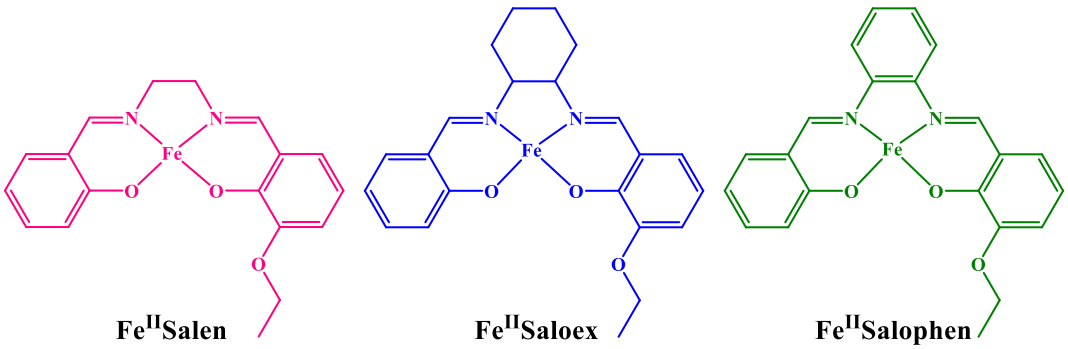

Fe^{II}Salen Fe^{II}Saloex Fe^{II}Salophen

Figure 1. Fe(II) complexes featuring non-symmetrical Schiff base ligands employed as photocatalysts in controlled radical photopolymerization.

2. Results and discussion

2.1. Synthesis and characterization of Fe(II) complexes

The synthesis of Fe(II)-Schiff base complexes has been investigated using different synthetic methods. In 2004, Lemos et al. reported the synthesis of a novel Fe(II) complex bearing a salen ligand, which was prepared by reacting $Fe(OAc)_2$ with the corresponding Schiff base in methanol.[35] In sequence, Abdallah et al. described the preparation of an Fe(II) complex with a salophen ligand, synthesized using a different precursor salt, $FeCl_2$, in good yield, in an ethanol–water mixture.[36] In 2016, Chapman et al. introduced an alternative electrochemical method for synthesizing Fe(II) complexes with salen ligands. By maintaining anhydrous and anoxic conditions during electrochemical synthesis, they successfully obtained highly air-sensitive and spectroscopically pure Fe(II)-salen complexes[37] Subsequent work of Chantarojsiri et al. reported the synthesis of Fe(II) complexes through the metalation of Schiff base ligands with $Fe(OAc)_2$ in methanol.[38]

In the present study, we initially attempted to synthesize Fe(II) complexes using traditional methods described in the literature, employing methanol as the solvent. However, these attempts were unsuccessful due to the oxidation of the complexes, which resulted from their high sensitivity to air and moisture. Consequently, we developed a new procedure in which Fe(II) complexes were synthesized via an equimolar reaction between $FeCl_2$ and the respective Schiff base ligands (ethoxy-salen, ethoxy-saloex, or ethoxy-salophen) under an argon atmosphere, using tetrahydrofuran (THF) as the solvent. The resulting Fe(II) complexes were obtained in good yields and characterized by FTIR, UV-Vis, fluorescence spectroscopy, elemental analysis, MALDI-TOF, and DFT calculations.

The FTIR spectra of the Fe(II) complexes and their respective free ligands showed numerous bands in the 2500–4000 cm^{-1} region (Figures S1–S3). The ν(C=N) bands were slightly shifted to lower wavenumbers, and strong bands at 306, 363, and 304 cm^{-1} (ethoxy-salen, -saloex, and -salophen, respectively) were observed, which are likely related to ν(Fe–N), confirming the coordination of the azomethine nitrogen atom. Coordination with the phenolic oxygen of the Schiff base is supported by the appearance of bands at 363, 450, and 358 cm^{-1} (ethoxy-salen, -saloex, and -salophen, respectively), associated with ν(Fe–O).

The elemental analysis (C, H and N) data accorded well with the calculated values. MALDI-TOF spectra of the **Fe^{II}Salen**, **Fe^{II}Saloex** and **Fe^{II}Salophen** complexes exhibited molecular ion signals at 366.5154, 420.5579, 414.4298 m/z, respectively (Figures S4–S6). These signals are consistent with the expected molecular weights of the Fe(II) complexes.

The optimized geometries of the three Fe(II) complexes, namely **Fe^{II}Salen**, **Fe^{II}Saloex**, and **Fe^{II}Salophen**, were determined using DFT calculations (see section 3.4 for further details). These structures are shown in Figure 2. The calculations confirm that the ground state of all three complexes corresponds to a quintet spin multiplicity (S = 2). The Schiff base ligands coordinate the Fe(II) centre in an (N,O,N,O)-tetradentate coordination mode. Across all three complexes, the Fe–N and Fe–O bond lengths are similar, indicating comparable coordination environments. Specifically, for **Fe^{II}Salen**, the bond lengths are 2.119 Å and 2.116 Å for N(1)–Fe and N(2)–Fe, respectively, and 1.921 Å and 1.917 Å for O(1)–Fe and O(2)–Fe. In **Fe^{II}Saloex**, the Fe–N bonds are slightly shorter 2.108 Å for N(1) and 2.107 Å for N(2), with Fe–O distances of 1.919 Å (O(1)) and 1.913 Å (O(2)). In turn, **Fe^{II}Salophen** shows Fe–N bond lengths of 2.121 Å (N(1))

and 2.122 Å (N(2)), slightly elongated than the previous ones, whereas the Fe–O bonds measure 1.922 Å (O(1)) and 1.915 Å (O(2)).

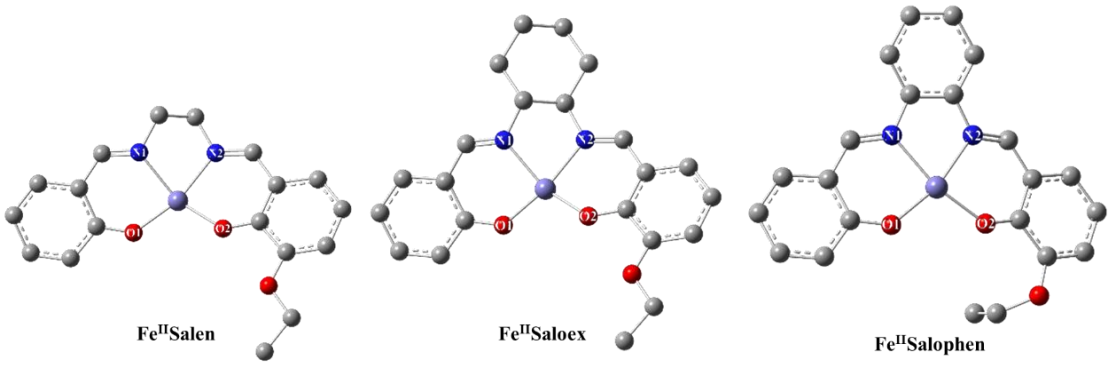

Figure 2. DFT optimized geometries for **Fe^{II}Salen**, **Fe^{II}Saloex** and **Fe^{II}Salophen** complexes. All geometries correspond to the quintet ground state (S = 2), which was found to be the lowest-energy spin configuration for each complex.

Variations in the ν(Fe–N) and ν(Fe–O) vibrational frequencies reflect subtle differences in the ligand field strength and geometric distortions. Notably, **Fe^{II}Saloex** exhibits the highest ν(Fe–O) value at 450 cm^{-1}, indicating stronger Fe–O interactions consistent with its slightly shorter bond lengths, while the lower ν(Fe–O) of **Fe^{II}Salophen** (358 cm^{-1}) aligns with its marginally elongated Fe–O distances, indicative of weaker metal–oxygen bonding.

The bond angles in these complexes illustrate their geometric distortions. The N(1)-Fe-O(1) and N(2)-Fe-O(2) angles range from 77.43 to 88.70°, with **Fe^{II}Saloex** exhibiting the highest symmetry among them. Interestingly, **Fe^{II}Salophen** shows a significantly larger N(2)-Fe-O(1) angle of 164.70° compared to 150.85° for **Fe^{II}Salen** and 151.19° for **Fe^{II}Saloex**. This difference suggests that **Fe^{II}Salophen** adopts a distorted square-planar geometry, while **Fe^{II}Salen** and **Fe^{II}Saloex** are better described by seesaw-like geometries.

This structural interpretation is further supported by the geometric parameter τ_4,[39] calculated using the formula $\tau_4 = 360 - (\alpha + \beta)/141$, where α and β are the two largest bond angles around the metal centre. The τ_4 values range from 1.00 for an ideal tetrahedral geometry to zero for a perfect square planar geometry, with intermediate values corresponding to seesaw or trigonal pyramidal geometries. For the **Fe^{II}Salen** and **Fe^{II}Saloex** complexes, τ_4 is 0.41, confirming their seesaw geometry, while a τ_4 value of 0.21 for **Fe^{II}Salophen** indicates a distorted square-planar geometry.[40,41] It is important to highlight that all bond lengths and angles around the Fe(II) centre are consistent with those typically observed in similar coordination compounds.

2.2. Optical properties of the Fe(II) complexes

The electronic absorption spectra of the Schiff base ligands and their complexes are presented in Figures S8-S9. In order to better understand their absorption features, a computational investigation of the electronic structure of the Fe(II) complexes was carried out. These were conducted using time-dependent density functional theory (TD-DFT) calculations (see section 3.4 for further details). Both simulated and experimental spectra were recorded over the 200–800 nm range (Figure 3 and Figures S11 and S12), with absorption maxima and their theoretical assignments summarized in Tables S4, S6 and S8. The main transitions are illustrated using natural transition orbitals (NTOs).[42]

The experimental absorption bands for **Fe^{II}Salen**, **Fe^{II}Saloex**, and **Fe^{II}Salophen** observed in the region between 221 and 302 nm are primarily attributed to $\pi \rightarrow \pi^*$ intraligand (IL) transitions within the Schiff base ligands. In turn, the bands observed in the 298–384 nm range can be majorly assigned to metal-to-ligand charge transfer (MLCT) transitions. For the Fe(II) complexes, the lowest unoccupied molecular orbital (LUMO) is predominantly composed by the π^* orbital of the ligand , while the highest

occupied molecular orbital (HOMO) mainly originates from the ligand π orbital, with a minor contribution from the Fe *d*-orbitals (Figure S13). Furthermore, these complexes exhibit considerable absorption in the 300–500 nm range (Figure 3), making them suitable as photocatalysts under LED@365 nm. For example, the computed absorption spectrum of **Fe^{II}Saloex** predicts an electronic transition at 366.6 nm, which is attributed to MLCT transitions. The molar absorptivities of **Fe^{II}Salen**, **Fe^{II}Saloex**, and **Fe^{II}Salophen** are 700, 2700, and 11200 L^{-1} cm^{-1}, respectively. Notably, Figure S10 includes the simulated absorption spectrum of **Fe^{II}Salen** in the singlet state, which can be directly compared with the quintet-state calculation shown in Figure 3. This comparison demonstrates better agreement with the experimental data when the quintet ground state is considered, further supporting its assignment as the true ground-state multiplicity.

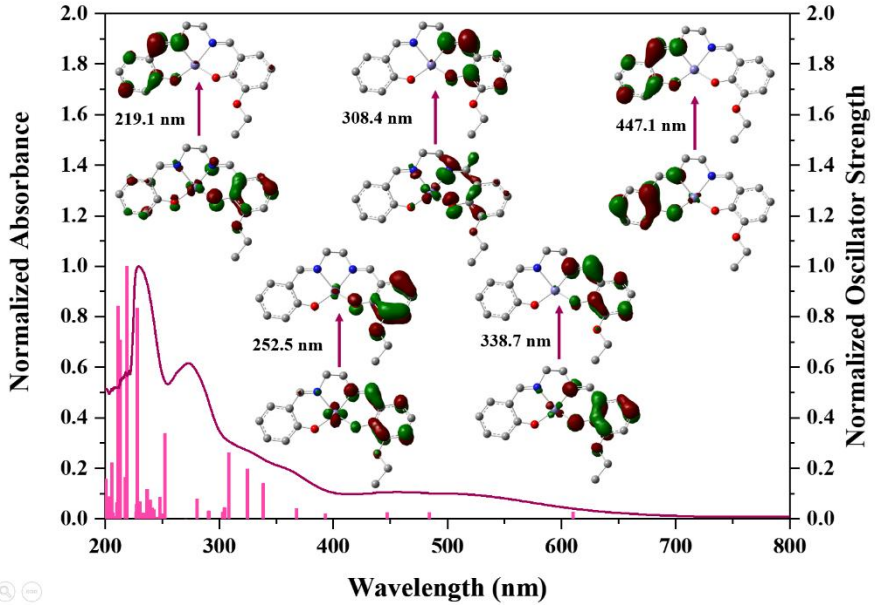

Figure 3. Normalized experimental (curve) and theoretical (vertical bars) electronic absorption spectrum for **Fe^{II}Salen** (ground state: quintet), along with the corresponding NTO orbitals for selected main transitions in the simulated spectrum.

The fluorescence properties of the Fe(II) complexes were investigated in CH_2Cl_2, THF, MeOH, and MeCN at 25 °C (Figures S14–S16). In CH_2Cl_2, the Fe(II) complexes exhibited an emission band at 400 nm upon excitation at 340 nm, emitting in the blue region of the spectrum. In more polar solvents, a bathochromic shift in both absorption and emission was observed, or emission was completely quenched. This behaviour can be attributed to the coordinating nature of the solvents, which likely influence the electronic structure of the Fe(II) complexes, altering their photophysical properties.[43,44] The highest emission intensity was observed in CH_2Cl_2 for all complexes. Furthermore, when monitoring emission at 365 nm, the excitation spectra revealed a band centred around 300 nm, which remained consistent throughout all complexes.

2.3. Controlled radical photopolymerization

A series of photoinduced Fe(II)-based CRP2 experiments using MA as the monomer were conducted under different conditions at 25 °C. Controlled experiments, designed by systematically omitting one reagent at a time, were performed to investigate the critical components influencing the polymerization process. Results indicated that polymerization did not occur without the Fe(II) complex or blue light irradiation, highlighting the essential roles of both factors in initiating CRP2 (entries 11 and 12, Table 1). To further assess the role of Fe(II) complexes as CRP2 photocatalysts, polymerization of MA was conducted in the presence of EBPA and TEA under LED@365 nm. The reaction was monitored until gelation occurred under different conditions, as presented in Table 1. These experiments provide essential information on the optimal conditions for Fe(II)-catalyzed CRP2.

An increase in the Fe/additives ratio from 0.02 to 0.04, while maintaining a monomer/additives ratio of 200, led to an increase in monomer conversion for **Fe^{II}Salen**

from 77 to 86% (entries 2 and 3, Table 1). For **Fe^{II}Saloex**, a decrease in monomer conversion from 61 to 31% was observed under the same conditions (entries 5 and 6, Table 1), whereas no polymerization occurred for **Fe^{II}Salophen** (entry 9, Table 1). The higher photocatalyst concentration can be directly linked to the generation of more initiating species, which react with the monomer, producing a greater number of polymer growth chains.[45] According to the Beer–Lambert law, light penetration decreases as optical density increases, a phenomenon known as the inner filter effect. This effect is influenced by the molar concentration of absorbing species, their molar absorptivity, and the optical path length. Therefore, the higher concentrations of **Fe^{II}Saloex** and **Fe^{II}Salophen**, combined with the deep brownish colour of the solutions, likely lead to increased light absorption by the non-photoinitiator species. This inner filter effect reduces the effective energy absorbed by the PIS throughout the solution, thereby diminishing the photopolymerization efficiency and the final degree of conversion.[46] In addition, the increase in the Fe/additive ratio also affected polymer uniformity, as evidenced by a slight increase in polydispersity (Đ) in all cases.

Table 1. Photoinduced Fe^{II}-catalyzed[a] CRP2 of MA at 25 ºC.

Entry	MA/EBPA/Fe^{II}/TEA	Time (min)	Conv.[b] (%)	M_n[c] (10^3 g mol^{-1})	Đ[d]
1	200/1/0/1	240	np	-	-
2	200/1/0.02/1	210	77	156	2.0
3	200/1/0.04/1	270	86	174	2.1
4	200/1/0.02/0.5	135	80	123	2.8
5	200/1/0.02/1	300	61	605	1.3
6	200/1/0.04/1	420	31	335	1.5
7	200/1/0.02/0.5	270	52	180	1.2
8	200/1/0.02/1	530	51	780	1.2
9	200/1/0.04/1	1200	np	-	-
10	200/1/0.02/0.5	300	70	480	1.3

11[e]	200/1/0.02/1	1200	np	-	-
12[f]	200/1/0.02/1	240	np	-	-

[a] **Fe^{II}Salen** was used in entries 2-4, **Fe^{II}Saloex** in 5-7, and **Fe^{II}Salophen** in 8-12. [b] The monomer conversions were determined by FTIR, with the following equation: $\text{conversion}\,(\%) = 100 \times (A_0 - A_t/A_0)$; np: no polymerization. [c] Number-average molecular weight. [d] Polydispersity index. [e] 420 nm LED as irradiation source. [f] Without light irradiation.

Regarding the additives, the Fe^{II}/TEA ratio was decreased from 1 to 0.5 for all Fe(II) complexes. For **Fe^{II}Salen**, this adjustment led to an increase in monomer conversion, accompanied by a rise in Đ from 2.0 to 2.8 and a reduction in photopolymerization time (entries 2 and 4, Table 1). In the case of **Fe^{II}Saloex**, the final conversion reached approximately 60%, with a reduction in photopolymerization time while maintaining control over the process (entries 5 and 7, Table 1). For **Fe^{II}Salophen**, a shorter photopolymerization time was observed, accompanied by an increase in conversion (entries 8 and 10, Table 1). These results suggest that the increased amount of EBPA likely enhances the generation of radical species responsible for initiating photopolymerization, thereby contributing to the observed reduction in the polymerization time for both complexes.

The kinetic behaviour of Fe(II) complexes in the CRP2 of MA was investigated using the MA/EBPA/Fe^{II}/TEA molar ratio of 200/1/0.02/1 for all complexes. The polymerization rate (R_p) as a function of MA conversion during photopolymerization catalyzed by Fe(II) complexes is shown in Figure 4. **Fe^{II}Salen** exhibited a significantly higher R_p compared to the other complexes, leading to faster polymerization and higher conversion. As a result, polymerization control was reduced, yielding a polymer with greater Đ (entry 2, Table 1). Furthermore, a post-peak decline was observed, attributed to reduced mobility due to the formation of long polymer chains and the gel effect at conversions greater than 40%. For **Fe^{II}Saloex** and **Fe^{II}Salophen**, a lower Rp was

10.1002/ejic.202500096

observed, and this slower polymerization led to a more gradual deceleration, forming a plateau rather than a sharp decline (Figure 4).

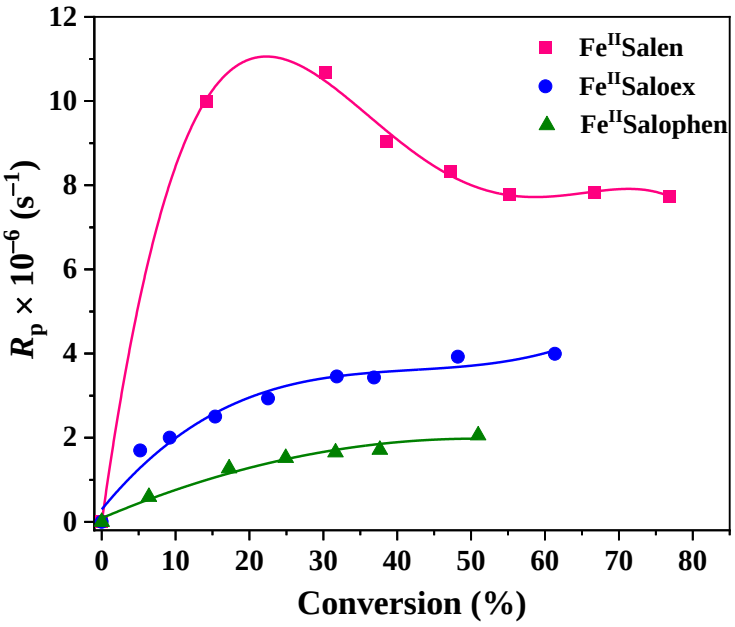

Figure 4. Dependence of R_p values on MA conversion for the CRP2 of MA using a molar ratio of 200/1/0.02/1 (MA/EBPA/Fe^{II}/TEA) at 25 °C.

In addition, a linear relationship between $ln([MA]_0/[MA]_t)$ and time, as shown in Figure 5, demonstrates that the polymerization rate follows pseudo first-order kinetics with respect to monomer concentration. This suggests that the concentration of radicals remained stable throughout the polymerization process for all complexes. The apparent rate constants (k_{app}) were of 5.3×10^{-3}, 2.8×10^{-3}, and 1.6×10^{-3} min^{-1} for **Fe^{II}Salen**, **Fe^{II}Saloex**, and **Fe^{II}Salophen**, respectively (Figure 5). These k_{app} values are consistent with the trends observed in the photopolymerization curves.

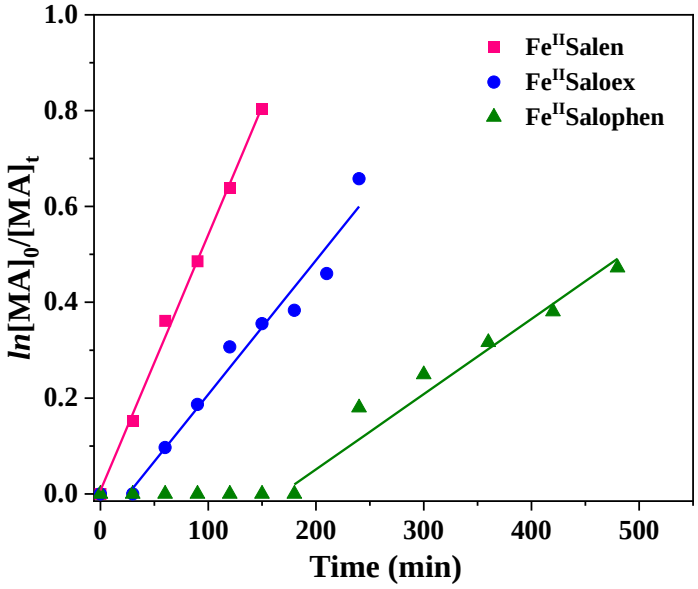

Figure 5. Kinetic plots of $ln([MA]_0/[MA]_t)$ *vs* time for the CRP2 of MA using a molar ratio of 200/1/0.02/1 (MA/EBPA/Fe^{II}/TEA) at 25 °C.

The optimal conditions were obtained using a MA/EBPA/Fe^{II}/TEA molar ratio of 200/1/0.02/1. **Fe^{II}Salen** exhibited good catalytic activity, achieving higher conversions but with reduced control over Đ. Although **Fe^{II}Salophen** exhibited low polydispersity, it proved ineffective under certain conditions. **Fe^{II}Saloex** reached higher conversion whereas maintaining lower polydispersity compared to its parent complexes. Telitel et al. investigated an Fe(II) complex bearing (NE)-4-nitro-N-(pyridin-2-ylmethylidene)aniline, achieving an MMA conversion of 51% with Đ = 2.5 using the same molar ratio applied to Fe^{II}-Schiff base complexes.[45] Interestingly, **Fe^{II}Saloex** exhibited superior performance, resulting in an MA conversion of 61% with Đ = 1.3. Following these results, a linear relationship between molecular weight and monomer conversion was observed for **Fe^{II}Saloex**, as shown in Figure 6. The nearly symmetrical shape of the molecular weight distribution curves demonstrates the dominance of the conditions for controlled radical photopolymerization, resulting a shift of the entire molecular weight distribution

10.1002/ejic.202500096

(MWD) of polyMA toward higher number-average molecular weight (M_n) values (Figure 6).

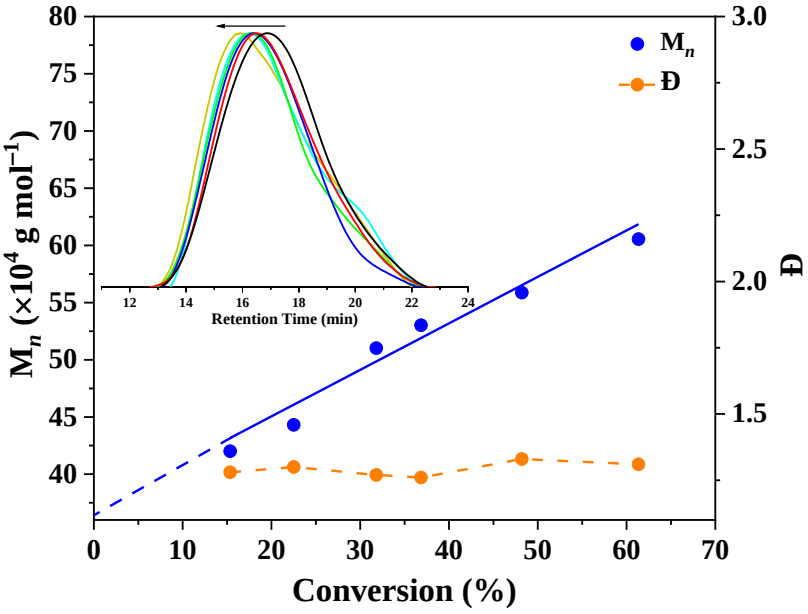

Figure 6. Photopolymerization of MA and SEC (size exclusion chromatography) chromatograms for polymers obtained using an MA/EBPA/**Fe^{II}Saloex**/TEA molar ratio of 200/1/0.02/1 under LED@365 nm.

To assess temporal control, experiments were conducted by intermittently switching the UV light ON and OFF. The photopolymerization of MA using a MA/EBPA/**Fe^{II}Saloex**/TEA molar ratio of 200/1/0.02/1 under LED@365 nm demonstrated that the reaction stopped when the LED was turned off (OFF mode). Furthermore, polymer formation occurred only after the UV light was turned ON periodically, resulting in higher conversions, as shown in Figure 7.

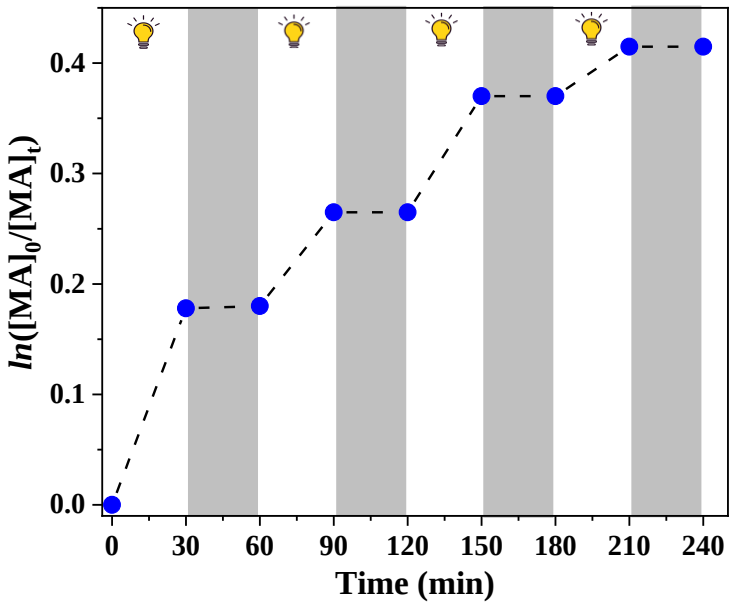

Figure 7. On-off experiment for CRP2 of MA using a molar ratio of 200/1/0.02/1 (MA/EBPA/**Fe^{II}Saloex**/TEA) under LED@365 nm.

2.4. Investigation of the mechanism

To shed a light into the chemical mechanism at play, the interaction between **Fe^{II}Saloex** and additives was investigated through steady-state photolysis experiments in CH_2Cl_2 under LED@365 nm at 25 °C. Initially, **Fe^{II}Saloex** was irradiated separately, and exhibited moderate stability. Even after extended periods of irradiation, only minor changes in the absorption spectra were observed (Figure S17). Next, the interaction of the **Fe^{II}Saloex**/TEA solution under irradiation was tested. As seen in Figure S18, only slight changes in the spectra occurred, suggesting that TEA has minimal influence on **Fe^{II}Saloex**. However, when EBPA was introduced, the spectra showed considerable changes, indicating a strong interaction between the additive and **Fe^{II}Saloex** under light (Figure 8). This is likely due to the formation of the ethyl phenylacetyl radical, which can initiate radical polymerization, along with an oxidized iron complex. This further confirms the important role of EBPA in influencing the behaviour of **Fe^{II}Saloex** during

photopolymerization, aligning with the overall findings regarding the catalytic activity of the photocatalyst.[16, 47]

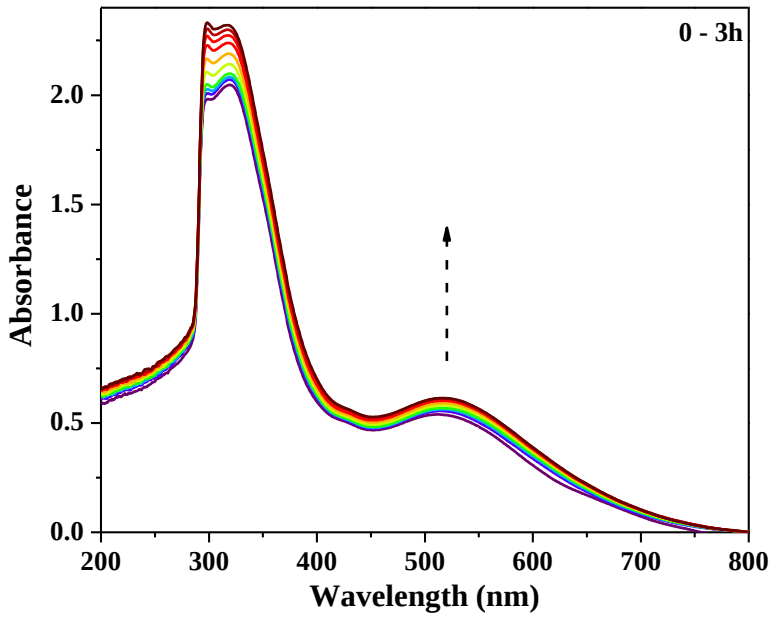

Figure 8. Steady-state photolysis of **Fe^{II}Salen** solutions with EBPA in CH_2Cl_2 under LED@365 nm.

Furthermore, the interaction between the photocatalyst and additives was investigated through fluorescence quenching, with the quantum yield determined using Stern–Volmer coefficients (Figure 9). Among the studied systems, the **Fe^{II}Saloex**/EBPA interaction exhibited the most significant fluorescence quenching, resulting in a Stern–Volmer constant (K_{SV}) of 93 M^{-1}, indicating a higher reactivity with EBPA (Figure 9a-b). The quantum yield (ϕ_{et}) associated with the electron transfer between Fe(II) and EBPA was calculated using the Stern–Volmer equation,[48] resulting in a value of 0.809. In contrast, the **Fe^{II}Saloex**/TEA interaction resulted in a lower K_{SV} value of 7.4 M^{-1} and ϕ_{et} values of 0.252, indicating a reduced quantum yield compared to EBPA (Figure 9c-d). These findings are consistent with the photolysis experiments.

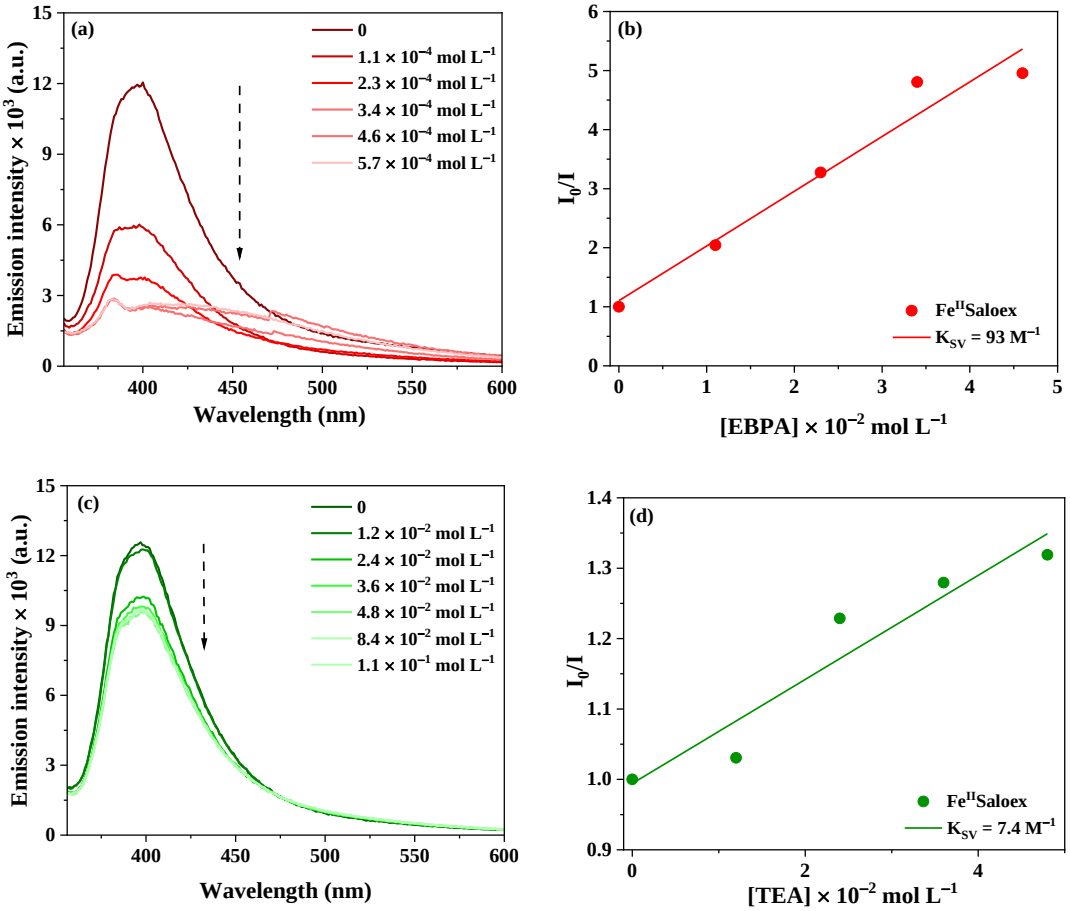

Figure 9. Fluorescence quenching of **Fe^{II}Saloex** with additives in CH_2Cl_2: (a) **Fe^{II}Saloex**/EBPA; (b) Stern–Volmer coefficient determination with EBPA; (c) **Fe^{II}Saloex**/TEA; (d) Stern–Volmer coefficient determination with TEA.

The CRP2 mechanism can occur through two different pathways, as reported in the literature.[14,41,49] One is the oxidative and the other is the reductive pathway. Both possibilities are represented in Scheme 1. In the first step (r1), the Fe(II) complex (PC), interacts with light, and is converted to its excited state (Fe(II)*). This species can interact with either EBPA (RBr) or TEA through two different reactions, r2 and r3, respectively. In r2, EBPA oxidises Fe(II)* to Fe(II)$^{\bullet+}$, that can be reduced back to the initial state by TEA (r2b); therefore, the PC is regenerated to Fe(II). In the reductive pathway, the Fe(II)*

species interacts first with TEA, forming $Fe(II)^{\bullet -}$ (r3), that can be regenerated to Fe(II) by EBPA (r3b). The $R^{\bullet}$ species that can be formed in r2 and r3b can initiate the polymerization (r6). It is worth noticing that the $TEA^{\bullet}_{(-H)}$ species can also interact with the monomer, contributing with an additional initiation route (r7). Another possibility is the reduction of $Fe(II)^{\bullet +}$ by $R(M)_n^{\bullet}$, once the reduction potential of Fe(III) is higher than that of EBPA (r3c). Therefore, the oxidative pathway was proposed due to the stronger interaction of Fe(II) with EBPA compared to TEA, which is consistent with both the experimental data and the literature [**Error! Bookmark not defined.**]. To gain further insights into this interaction, the free energy change (ΔG_{et}) associated with the photoinduced electron transfer from the Fe(II) complexes to EBPA was estimated using the classical Rehm–Weller equation[45,48]. The electrochemical potentials and excited-state energies of the photocatalysts were determined by cyclic voltammetry and UV–Vis absorption and emission spectroscopy (Figures S19 and S20). The ΔG_{et} values calculated for **Fe^{II}Salen**, **Fe^{II}Saloex**, and **Fe^{II}Salophen** were –1.91, –1.90, and –1.98 eV, respectively. The negative values obtained for all complexes confirm the thermodynamic feasibility of electron transfer to EBPA from the excited states, thus supporting the proposed oxidative pathway.

10.1002/ejic.202500096

(r1) $Fe(II) \rightarrow Fe(II)^{*}$ ($h\nu$)

(r2) $Fe(II)^{*} + RBr \rightarrow Fe(II)^{\bullet+}/Br^{-} + R^{\bullet}$

(r3) $Fe(II)^{*} + TEA \rightarrow Fe(II)^{\bullet-} + TEA^{\bullet+} \rightarrow Fe(II)^{\bullet-} + TEA^{\bullet}_{(-H)} + H^{+}$

(r2b) $Fe(II)^{\bullet+} + TEA \rightarrow Fe(II) + TEA^{\bullet}_{(-H)} + H^{+}$

(r3b) $Fe(II)^{\bullet-} + RBr \rightarrow Fe(II) + RBr^{\bullet-} \rightarrow Fe(II) + R^{\bullet} + Cl^{-}$

(r6) $R^{\bullet} + nM \rightarrow R(M)_n^{\bullet}$

(r7) $TEA^{\bullet}_{(-H)} + nM \rightarrow TEA_{(-H)}\text{-}(M)_n^{\bullet}$

(r3c) $Fe(II)^{\bullet+}/Br^{-} + R(M)_n^{\bullet} \rightarrow Fe(II) + R(M)_n\text{-}Br$

Scheme 1. Proposed reactions for the CRP2 steps mechanisms of the Fe(II)/EBPA/TEA redox combination.

10.1002/ejic.202500096

Conclusions

The synthesis of Fe(II) complexes bearing non-symmetric Schiff base ligands was reported, yielding the target complexes in good yields. Fe(II) complexes were fully characterized using various spectroscopic techniques, including FTIR, UV-Vis, and fluorescence spectroscopy. Their optimized geometries were determined through density functional theory calculations, with theoretical results aligning well with the experimental data. The simulated spectra provided a detailed understanding of the main electronic transitions in the complexes. Given their significant absorption in the visible range, these Fe(II) complexes were evaluated as photocatalysts for controlled radical photopolymerization (CRP2) under LED irradiation. **Fe^{II}Saloex** demonstrated the best performance, achieving high monomer conversion, a linear kinetic profile, and low polydispersity. Additionally, the interaction between the photocatalyst and additives was examined, revealing that the Fe(II)*/EBPA interaction was more effective than Fe(II)*/TEA. Based on these findings and spectroscopic data, an oxidative mechanism pathway for the photopolymerization was proposed. These findings highlight the potential of these Fe(II) complexes as effective photocatalysts for CRP2, paving the way for the development of advanced materials with tailored properties.

3. Experimental

3.1. General remarks

All reagents were purchased from Aldrich Chemical Co. All reactions and manipulations were performed under a nitrogen atmosphere using standard Schlenk techniques. Methyl acrylate (MA) was washed three times with 5% NaOH solution at an equimolar ratio with water. After that, the monomer was dried over anhydrous $CaCl_2$ and stored at –18 ºC under nitrogen. The compounds *o*-phenylenediamine, ethylenediamine, cyclohexane-1,2-diamine, trimethylamine, 3-ethoxysalicylaldehyde, salicylaldehyde and ethyl α-bromophenylacetate (EBPA) were used without further purification. The ligands ethoxy-salen, ethoxy-saloex, and ethoxy-salophen were synthetized as reported in the literature,[31,32,50-52] and their purity was confirmed by satisfactory spectroscopic methods.

3.2. Analyses

Chemical shifts are reported in ppm relative to tetramethylsilane (TMS) as an internal standard. Monomer conversion was determined by measuring the residual monomer concentration using infrared spectroscopy. IR spectra were obtained on a PerkinElmer Frontier instrument equipped with a diamond ATR module, and recorded in the 4000–250 cm^{-1} range at a resolution of 4 cm^{-1}. Each spectrum was acquired over 64 s at 298 K. UV-Vis measurements were performed using a Shimadzu UV-2600 spectrophotometer with 1 cm path length quartz cells. CH_2Cl_2 solutions of the complexes at a concentration of 0.5 mmol L^{-1} were used for these measurements. MALDI-TOF measurements were carried out using a Bruker Daltonic Autoflex III Smartbean instrument. Molecular weights and molecular weight distribution of the polymers were determined by gel permeation chromatography (GPC) using a Shimadzu Prominence LC system equipped with an LC-20AD pump, a DGU-20A5 degasser, a CBM-20A

communication module, a CTO-20A oven set to 40 ºC, and a RID-10A detector. The system was equipped with two Shimadzu GPC-805 columns (30 cm, Ø = 8.0 mm). Retention times were calibrated using monodispersed poly(methyl methacrylate) standards in HPLC-grade THF as the eluent at 40 ºC, with a flow rate of 1.0 mL min^{-1}. The polydispersity index (Đ) is defined as the ratio of the weight-average molecular weight (M_w) to the number-average molecular weight (M_n), i.e., $Đ = M_w/M_n$. For steady-state photolysis experiments, solutions of the iron complexes, either alone or in the presence of EBPA, TEA, or both, were irradiated with an LED light source at 365 nm. UV-Vis spectra were recorded at different time intervals during irradiation. The molar concentrations of the complex and additives matched those used in the photopolymerization conditions, namely 200/1/0.02/1 (MA/EBPA/Fe^{II}/TEA).

3.3. Synthesis of Fe(II)–Schiff bases complexes

The **Fe^{II}Salen**, **Fe^{II}Saloex**, and **Fe^{II}Salophen** complexes were synthetized following the same procedure. To a two-necked flask containing the Schiff base (1 eq) and $FeCl_2$ (1 eq), 5 mL of THF was transferred through a cannula under an argon atmosphere. The solution immediately acquired a dark red colour. The system was then placed under stirring and reflux conditions at 70°C for 2 hours. After solvent removal, the resulting red precipitate was washed with pentane and dried under reduced pressure for several hours, yielding the desired complexes as wine-coloured powders.

Fe^{II}Salen: Yield: 79% (92.6 mg). a) FTIR (cm^{-1}): 3000-2825 ν(C−H), 1612 ν(C=N), 1247 ν(C−O−C), 1078 ν(C−O), 458 ν(Fe−O), 350 ν(Fe−N); b) (CH_2Cl_2, nm (mol L^{-1} cm^{-1}), λ_{max} (ε) = 230 (2138), 272 (1334), 325 (584), 360 (426), 455 (232), 515 (212); c) MALDI-TOF: m/z calcd for $C_{18}H_{18}FeN_2O_3$: 366.07 g mol^{-1}; found: 366.5154; d) Elemental analysis calcd (%) for $C_{18}H_{18}FeN_2O_3$: C 59.04; H 4.95; N 7.65%; found: C 59.23; H 5.12; N 7.89%.

Fe^{II}Saloex: Yield: 92% (124 mg). a) FTIR (cm^{-1}): 3160-2800 ν(C−H), 1620 ν(C=N), 1249 ν(C−O−C), 1079 ν(C−O), 450 ν(Fe−O), 363 ν(Fe−N); b) (CH_2Cl_2, nm (mol L^{-1} cm^{-1}), λ_{max} (ε) = 272 (1990), 325 (836), 360 (652), 455 (328), 515 (298); c) MALDI-TOF: m/z calcd for $C_{22}H_{24}FeN_2O_3$: 420.11 g mol^{-1}; found: 420.5579; d) Elemental analysis calcd (%) for $C_{22}H_{24}FeN_2O_3$: C 62.87; H 5.76; N 6.67%; found: C 63.11; H 5.92; N 6.84%.

Fe^{II}Salophen: Yield: 85% (113 mg). a) 3050-2822 ν(C−H), 1591 ν(C=N), 1238 ν(C-O−C), 1043 ν(C−O), 358 ν(Fe−O), 304 ν(Fe−N); b) (CH_2Cl_2, nm (mol L^{-1} cm^{-1}), λ_{max} (ε) = 230 (1635), 272 (982), 325 (1236), 360 (681), 455 (191), 515 (128); c) MALDI-TOF: m/z calcd for $C_{22}H_{18}FeN_2O_3$: 414.07 g mol^{-1}; found: 414.4298; d) Elemental analysis calcd (%) for $C_{22}H_{24}FeN_2O_3$: C 63.79; H 4.38; N 6.76%; found: C 63.91; H 4.49; N 6.99%.

3.4. Theoretical calculations

All DFT calculations in this work were conducted using the ORCA 5.0 quantum chemistry package.[53] A computational study was carried out to evaluate all possible spin multiplicities (singlet, triplet, and quintet) for the Fe(II)–Schiff base complexes. In particular, the geometric parameters obtained for the singlet and quintet states are presented in Tables S1 and S2, respectively. Gas-phase geometry optimizations were

carried out using the unrestricted DFT method, when applicable. The hybrid PBE0 functional[54,55] was employed for both optimization and single-point energy calculations, with def2-SVP basis set applied to C, H, N, and O atoms and def2-TZVP for Fe.[56] Dispersion interactions were accounted for using Grimme's D3 correction[57] with the Becke–Johnson (BJ) damping function.[58] To reduce computational cost, the resolution-of-the-identity approximation for Coulomb integrals (RI-J) combined with the chain-of-spheres-exchange (COSX) method (RIJCOSX)[59,60] was applied, utilizing the def2/J auxiliary basis sets. All calculations were performed with tight convergence criteria. Harmonic vibrational frequencies were computed at this level of theory to ensure that the stationary points as true minima, signifying equilibrium structures on the potential energy surfaces. This further ensured that imaginary frequencies were not generated in the minimum structures. Selected bond distances and bond angles from these calculations are listed in Table S2. Among the tested spin states, the quintet state (four unpaired electrons) yielded the lowest energy values: $E = -2293.667795$, -2449.443811 and -2445.829828 Hartree (**Fe^{II}Salen, Fe^{II}Saloex** and **Fe^{II}Salophen**, respectively). This finding aligns with a recent benchmark study, which indicates that Fe(II) complexes with coordination number 4 predominantly adopt an open-shell configuration, with the quintet state being the most common ground state.[61] The corresponding energies for the singlet state were $E = -2293.604986$, -2449.381907, and -2445.763632 Hartree, which are 39.4, 38.8, and 41.5 kcal mol^{-1} higher than the respective quintet states. For the triplet states, the energies were –2293.658249, –2449.434667, and –2445.824268 Hartree, corresponding to 6.0, 5.7, and 3.5 kcal mol^{-1} higher than the respective quintet states. Based on these results, all subsequent calculations were carried out using the quintet state. To theoretically predict the UV-Vis spectra of all complexes, TD-DFT calculations were performed at the ωB97X-D3(BJ)/def2-SVP [Fe: def2-TZVP] level.[62] This computational approach was

chosen because its long-range-separated functional provides a more balanced treatment of charge transfer excitations, making it particularly suitable for describing electron excitations,[63,64] including those of organometallic systems.[65-67] The theoretical assignments of the singlet and quintet states are summarized in Tables S3–S8. Natural transition orbitals (NTOs)[42] were generated as cube files using the ORCA program and visualized with GaussView 6.[68]

3.5. CRP2 procedure

The photoinduced Fe(II)-catalyzed CRP2 of MA was investigated using varying proportions of the monomer, initiator (EBPA), co-initiator (TEA) and Fe(II) complex. A 365 nm LED light source was used for irradiation. Initially, a Schlenk flask containing the Fe(II) complex was degassed by performing three vacuum/nitrogen cycles. Then, a mixture of MA, EBPA and TEA was added, and the system was sealed, placed in a stirring apparatus, and exposed to LED@365 nm (10 W cm^{-2}) at 25 ºC. At specific reaction intervals, 0.1 mL aliquots were extracted, dissolved in 1 mL of THF, and analysed by FTIR to determine monomer conversion and by GPC to assess polymer molecular weights and molecular weight distributions.

Acknowledgements

BEG, VPCJ, NMP are indebted to the financial support from FAPESP, grant #2021/11873-1, grant #2021/13128-1, and #2021/11741-8, respectively, São Paulo Research Foundation (FAPESP). The authors acknowledge the financial support provided by PROPe/UNESP through the public call Edital 04/2024. The financial support of CNPq (Proc. 8881.934179/2024-01) is gratefully acknowledged (sandwich doctoral fellowship to MLBF). This article is based upon work from the COST Action CA20129 - Multiscale

Irradiation and Chemistry Driven Processes and Related Technologies (MultIChem), supported by COST (European Cooperation in Science and Technology). MLBF and FF are grateful to the computational support provided by the University of Kent and Julius-Maximilians-Universität Würzburg.

References

[1] C. J. Fristrup; K. Jankova; S. Hvilsted, *Soft Matter* **2009**, *5*, 4623−4634.

[2], Z. Dong, H. Cui, H. Zhang, F. Wang, X. Zhan, F. Mayer, B. Nestler, M. Wegener, P. A. Levkin, *Nat. Commun* **2021**, *12*, 247.

[3] P. Glöckner, *Vincentz Network GmbH & Co KG* **2009**.

[4] R. Labella, P. Lambrechts, B. V. Meerbeek, G. Vanherle, *Dent Mater.* **1999**, *15*, 128−137

[5] W. Li, L. S. Mille, J. A. Robledo, T. Uribe, V. Huerta, Y. S. Zhang, *Adv. Healthc. Mater.* **2020**, *9*, 2000156.

[6] C. Idumah, *Polym. Compos.* **2020**, *29*, 246−258.

[7] M. Mahmoudpour, M. Torbati, M. Mousavi, M. Guardia, J. E. N. Dolatabadi, *TrAC, Trends Anal. Chem.* **2020**, *129*, 115943.

[8] M. Chen, M. Zhong, J. A. Johnson, *Chem. Rev.* **2016**, *17*, 10167−10211.

[9] C. Aydogan, G. Yilmaz, A. Shegiwal, D. M. Haddleton, Y. Yagci, *Angew. Chem.* **2022**, *134*, e202117377.

[10] N. Zivic, M. Bouzrati-Zerelli, A. Kermagoret, F. Dumur, J. Fouassier, D. Gigmes, J. Lalevée, *ChemCatChem* **2016**, *8*, 1617−1631.

[11] S. Telitel, F. Dumur, M. Lepeltier, D. Gigmes, J. Fouassier, J. Lalevée, *C. R. Chim.* **2016**, *19*, 71−78.

[12] J. Lalevée, M. Peter, F. Dumur, D. Gigmes, N. Blanchard, M. Tehfe, F. Morlet-Savary, J. Fouassier, *Chem. - Eur. J.* **2011**, *17*, 15027−15031.

[13] Y. Chen, Z. Hu, D. Xu, Y. Yu, X. Tang, H. Guo, *Macromol. Chem. Phys.* **2015**, *216*, 1055−1060.

[14] P. Xiao, J. Zhang, D. Campolo, F. Dumur, D. Gigmes, J. P. Fouassier, J. Lalevée, *J. Polym. Sci., Part A:Polym. Chem.* **2015**, *53*, 2673−2684.

[15] M. Tehfe, L. Ma, B. Graff, F. Morlet-Savary, J. Fouassier, J. Zhao, J. Lalevée, Macromol. Chem. Phys. **2012**, *213*, 2282−2286.

[16] J. Zhang, D. Campolo, F. Dumur, P. Xiao, J. P. Fouassier, D. Gigmes, J. Lalevée, J. Polym. Sci., Part A:Polym. Chem. **2014**, *53*, 42−49.

[17] C. Dietlin, S. Schweizer, P. Xiao, J. Zhang, F. Morlet-Savary, B. Graff, J. Fouassier, J. Lalevée, *Polym. Chem.* **2015**, *6*, 3895−3912.

[18] X. Zhigang, D. He, X. Xie, *Polym. Chem.* **2015**, *6*, 1660−1687.

[19] M. B. A. Afonso, T. R. Cruz, Y. F Silva, J. C. A. Pereira, A. E. H. Machado, B. E. Goi, B. S. Lima-Neto, V. P. Carvalho-Jr, *J. Org. Chem.* **2017**, *851*, 225−234.

[20] A. H. S. Idehara, P. D. S. Gois, H. Fernandez, B. E. Goi, A. E. H. Machado, B. S. Lima-Neto, Valdemiro P. Carvalho-Jr, *J. Mol. Catal.* **2018**, *448*, 135−143.

[21] T. R. Cruz, E. A. Silva, D. P. Oliveira, D. M. Martins, P. D. S. Gois, A. E. H. Machado, P. I. S. Maia, B. E. Goi, B. S. Lima-Neto, V. P. Carvalho-Jr, *Appl. Organomet. Chem.* **2020**, *34*, e5602.

[22] P. D. S. Gois, T. R. Cruz, D. M. Martins, A. E. H. Machado, A. L. Bogado, B. S. Lima-Neto, B. E. Goi, V. P. Carvalho-Jr, *J. Mol. Struct.* **2019**, *1198*, 126874.

[23] P. Borim, B. S. Lima-Neto, B. E. Goi, V. P. Carvalho-Jr. *Inorganica Chim. Acta* **2017**, *456*, 171−178.

[24] T. R. Cruz, R. A. N. Silva, A. E. H. Machado, B. S. Lima-Neto, B. E. Goi, V. P. Carvalho-Jr. *NJC* **2019**, *43*, 6220−6227.

[25] T. R. Cruz, P. Borim, B. E. Goi, J. L. S. Sá, B. S. Lima-Neto, V. P. Carvalho-Jr. *J. Polym. Res.* **2017**, *24*, 1−8.

[26] B. A. Riga, M. D. Neves, A. E. H. Machado, D. M. S. Araújo, J. R. Souza, O. R. Nascimento, V. T. Santana, C. C. S. Cavalheiro, V. P. Carvalho-Jr, B. E. Goi, *Inorganica Chim. Acta* **2018**, *471*, 620−629.

[27] T. T. Silva, Y. F. Silva, A. E. H. Machado, P. I. S. Maia, C. R. B. Tasso, B. S. Lima-Neto, J. L. S. Sá, V. P. Carvalho-Jr, N. C. Batista, B. E. Goi. *J. Macromol. Sci., Part A:Pure Appl. Chem.* **2019**, *56*, 1132−1140.

[28] Y. F. Silva, B. A. Riga, V. M. Deflon, J. R. Souza, L. H. F. Silva, A. E. Machado, P. I. S. Maia, V. P. Carvalho-Jr, B. E. Goi, *J. Coord. Chem.* **2018**, 71, 3776−3789.

[29] B. A. Riga, Y. F. Silva, O. R. Nascimento, A. E. H. Machado, V. P. Carvalho-Jr, B. E. Goi, *Polyhedron* **2020**, *192*, 114870.

[30] P. K. Hashimoto, L. F. Oliveira, B. A. Riga-Rocha, A. E. H. Machado, V. T. Santana, O. R. Nascimento, V. P. Carvalho-Jr, B. E. Goi, *NJC* **2021**, *45*, 10109−10117.

[31] L. F. Oliveira, C. Bignardi, N. M. Pesqueira, B. A. Riga-Rocha, A. E. H. Machado, V. P. Carvalho-Jr, B. E. Goi, *Eur. Polym. J* **2021**, *159*, 110757.

[32] C. Bignardi, L. F. Oliveira, N. M. Pesqueira, B. A. Riga-Rocha, A. E. H. Machado, V. P. Carvalho-Jr, B. E. Goi, *J. Photochem. Photobiol. A C* **2022**, *423*, 113595.

[33] N. M. Pesqueira, C. Bignardi, L. F. Oliveira, A. E. H. Machado, V. P. Carvalho-Jr, B. E. Goi, *J. Photochem. Photobiol. A C* **2023**, *437*, 114443.

[34] N. M. Pesqueira, K. H. Lira, C. Bignardi, M. K. C. Silva, T. F. Silva, A. E. H. Machado, O. R. Nascimento, V. P. Carvalho-Jr, B. E. Goi, *Appl. Organomet. Chem.* **2024**, *38*, e7495.

[35] F. C. D. Lemos, M. Muraro, J. Zukerman-Schpector, É. T. G. Cavalheiro, E. R. Dockal, *J. Therm. Anal. Calorim.* **2004**, *75*, 599−606.

[36] S. M. Abdallah, G. G. Mohamed, M. A. Zayed, M. S. Abou El-Ela, *Spectrochim. Acta A Mol. Biomol. Spectrosc.* **2009**, *73*, 833−840.

[37] M. R. Chapman, S. E. Henkelis, N. Kapur, B. N. Nguyen, C. E. Willians, *ChemistryOpen*, **2016**, *5*, 351−356.

[38] T. Chantarojsiri, J. W. Ziller, J. Y. Yang, *Chem. Sci.*, **2018**, *9*, 2567−2574.

[39] L. Yang, D. R. Powell, R. P. Houser, Dalton Trans. **2007**, 955−964.

[40] R. Takjoo, P. Ramasami, L. Rhyman, M. Ahmadi, H. A. Rudbari, G. Bruno, *J. Mol. Struct.* **2022**, *1255*, 132388.

[41] J. Lalevée, S. Telitel, P. Xiao, M. Lepeltier, F. Dumur, F. Morlet-Savary, D. Gigmes, J. Fouassier, *Beilstein J. Org. Chem.* **2014**, *10*, 863−876.

[42] R. L. Martin, *J. Chem. Phys.* **2003**, *118*, 4775−4777.

[43] D. M. Roundhill, *Photochemistry and photophysics of metal complexes*, Springer Science & Business Media, **1994**.

[44] B. M. França, S. S. C. Oliveira, L. O. P. Souza, T. P. Mello, A. L. S. Santos, J. S. B. Forero, *Dyes Pigm.* **2022**, *198*, 110011.

[45] S. Telitel, F. Dumur, D. Campolo, J. Poly, D. Gigmes, J. Fouassier, J. Lalevée, *J. Polym. Sci., Part A:Polym. Chem.* **2015**, *54*, 702−713.

[46] P. Garra, C. Dietlin, F. Morlet-Savary, F. Dumur, D. Gigmes, J. Fouassier, J. Lalevée, *Polym. Chem.* **2017**, *8*, 7088−7101.

[47] F. Nzulu, S. Telitel, F. Stoffelbach, B. Graff, F. Morlet-Savary, J. Lalevée, L. Fensterbank, J. Goddard, C. Ollivier, *Polym. Chem.* **2015**, *6*, 4605−4611.

[48] N. M. Pesqueira, F. Morlet-Savary, M. Schimitt, V. P. Carvalho-Jr, B. E. Goi, J. Lalevée, *Eur. Polym. J.* **2024**, *216*, 113279.

[49] J. Lalevée, M. Tehfe, F. Morlet-Savary, B. Graff, F. Dumur, D. Gigmes, N. Blanchard, J. Fouassier, *Chimia* **2012**, *66*, 439−441.

[50] K. Nejati, Z. Rezvani, M. Seyedahmadian, *Dyes Pigm.* **2009**, *83*, 304−311.

[51] Y. Shimogori, T. Hamamatsu, T. Fujinami, H. Hagiwara, N. Matsumoto, N. Re, J. Mrozinski, Y. Ishikawa, A. Igashira-Kamiyama, T. Konno, *Polyhedron* **2011**, *30*, 1127−1133.

[52] A. A. Nejo, G. A. Kolawole, A. R. Opoku, C. Muller, J. Wolowska, *J. Coord. Chem.* **2009**, *62*, 3411−3424.

[53] F. Neese, *Wiley Interdiscip. Rev. Comput. Mol. Sci.* **2022**, *12*, e1606.

[54] M. Ernzerhof, G. E. Scuseria, *J. Chem. Phys.* **1999**, *110*, 5029−5036.

[55] C. Adamo, V. Barone, *J. Chem. Phys.* **1999**, *110*, 6158−6170.

[56] F. Weigend, R. Ahlrichs, *Phys. Chem. Chem. Phys.* **2005**, *7*, 3297−3305.

[57] S. Grimme, J. Antony, S. Ehrlich, H. Krieg, *J. Chem. Phys.* **2010**, *132*, 154104.

[58] S. Grimme, S. Ehrlich, L. Goerigk, *J. Comput. Chem.* **2011**, *32*, 1456−1465.

[59] F. Neese, *J. Comput. Chem.* **2003**, *24*, 1740−1747.

[60] F. Neese, F. Wennmohs, A. Hansen, U. Becker, *Chem. Phys.* **2009**, *356*, 98−109.

[61] Y. Cho, R. Laplaza, S. Vela, C. Corminboeuf, *Digit. Discov.* **2024**, *3*, 1638−1647.

[62] A. Najibi, L. Goerigk, *J. Chem. Theory Comput.* **2018**, *14*, 5725−5738.

[63] L. Craciunescu, S. Wirsing, S. Hammer, K. Broch, A. Dreuw, F. Fantuzzi, V. Sivanesan, P. Tegeder, B. Engels, *J. Phys. Chem. Lett.* **2022**, *13*, 3726−3731.

[64] L. Craciunescu, M. Asbach, S. Wirsing, S. Hammer, F. Unger, K. Broch, F. Schreiber, G. Witte, A. Dreuw, P. Tegeder, F. Fantuzzi, B. Engels, *J. Chem. Theory Comput.* **2023**, *19*, 9369−9387.

[65] M. Yáñez-S, S. A. Moya, C. Zúñiga, G. Cárdenas-Jirón, *Comput. Theor. Chem*. **2017**, *1118*, 65−74.

[66] D. Das, A. Roy, S. Sutradhar, F. Fantuzzi, B. N. Ghosh, *Sens. Diagn.* **2023**, *2*, 1649−1657.

[67] C. P. Souza, F. Fantuzzi, *Computational strategies for modeling excited states in organometallic chemistry*, *Vol. 45* (Eds.: BAKEWELL, C.; OWEN, G.R.; COSTA, N.; MUSGRAVE, R.). Organometallic Chemistry: London: Royal Society of Chemistry, **2024**., p. 271.

[68] R. Dennington, T. A. Keith, J. M. Millam, GaussView, Version 6. Shawnee Mission, KS: Semichem Inc., **2016**.